



# 1 Natural marine bromoform emissions in the fully coupled ocean- 2 atmosphere-model NorESM2

3  
4 Dennis Booge<sup>1,2</sup>, Jerry F. Tjiputra<sup>3</sup>, Dirk J. L. Olivie<sup>4</sup>, Birgit Quack<sup>1</sup> and Kirstin Krüger<sup>2</sup>

5 <sup>1</sup>GEOMAR Helmholtz Centre for Ocean Research Kiel, Kiel, 24105, Germany

6 <sup>2</sup>Department of Geosciences, Section of Meteorology and Oceanography, University of Oslo, Oslo, 0371, Norway

7 <sup>3</sup>NORCE Norwegian Research Centre and Bjerknes Centre for Climate Research, Bergen, 5007, Norway

8 <sup>4</sup>Norwegian Meteorological Institute, Oslo, 0313, Norway

9 *Correspondence to:* Dennis Booge (dbooge@geomar.de) and Kirstin Krüger (kkrueger@geo.uio.no)

10 **Abstract.** Oceanic bromoform (CHBr<sub>3</sub>) is an important precursor of atmospheric bromine. Although highly relevant for  
11 the future halogen burden and ozone layer in the stratosphere, the global CHBr<sub>3</sub> production in the ocean and its emissions  
12 are still poorly constrained in observations and are mostly neglected in climate models. Here, we newly implement marine  
13 CHBr<sub>3</sub> in the state-of-the-art Norwegian Earth System Model (NorESM2) with fully coupled ocean-sea-ice-atmosphere  
14 biogeochemistry interactions. Our results are validated with oceanic and atmospheric observations from the HalOcAt  
15 (Halocarbons in the Ocean and Atmosphere) data base. The simulated mean oceanic concentrations ( $6.61 \pm 3.43$  pmol L<sup>-1</sup>)  
16 are in good agreement with observations in open ocean regions ( $5.02 \pm 4.50$  pmol L<sup>-1</sup>), while the mean atmospheric  
17 mixing ratios ( $0.76 \pm 0.39$  ppt) are lower than observed but within the range of uncertainty ( $1.45 \pm 1.11$  ppt). The NorESM2  
18 ocean emissions of CHBr<sub>3</sub> ( $214$  Gg yr<sup>-1</sup>) are in the range of or higher than previously published estimates from bottom-  
19 up approaches but lower than estimates from top-down approaches. Annual mean emissions are mostly positive (sea-to-  
20 air), driven by oceanic concentrations, sea surface temperature and wind speed, dependent on season and location. During  
21 low-productivity winter seasons, model results imply some oceanic regions in high latitudes as sinks of atmospheric  
22 CHBr<sub>3</sub>, because of its elevated atmospheric mixing ratios. We further demonstrate that key drivers for the oceanic and  
23 atmospheric CHBr<sub>3</sub> variability are spatially heterogeneous. In the tropical West Pacific, which is a hot spot for oceanic  
24 bromine delivery to the stratosphere, wind speed is the main driver for CHBr<sub>3</sub> emissions on annual basis. In the North  
25 Atlantic as well as in the Southern Ocean region the atmospheric and oceanic CHBr<sub>3</sub> variabilities are interacting during  
26 most of the seasons except for the winter months where sea surface temperature is the main driver. Our study provides  
27 improved process understanding of the biogeochemical cycling of CHBr<sub>3</sub> and more reliable natural emission estimates  
28 especially on seasonal and spatial scales compared to previously published model estimates.

## 29 1 Introduction

30 Bromoform (CHBr<sub>3</sub>) from the ocean is the most important organic compound for atmospheric bromine with an  
31 atmospheric lifetime of ~2-4 weeks (Carpenter and Liss, 2000; Quack and Wallace, 2003; Salawitch, 2006; Papanastasiou  
32 et al., 2014). As a reactive halogenated compound, it belongs to the very short-lived substances (VSLs) with lifetimes of  
33 less than 6 months in the atmosphere (Law et al., 2007). In the tropics, VSLs are rapidly lifted to the stratosphere by  
34 tropical deep convection (Sala et al., 2014; Navarro et al., 2015; Fuhlbrügge et al., 2016), where they contribute up to  
35 ~25% to stratospheric bromine (Dorf et al., 2006 and following work). Bromine is ~60 times more efficient in depleting  
36 lower stratospheric ozone than chlorine and significantly contributes to ozone depletion in the lower stratosphere (Daniel  
37 et al., 1999; Sinnhuber et al., 2009; Montzka et al., 2011; Villamayor et al., 2023) with potential impacts on the radiation  
38 budget of the atmosphere from  $-0.02$  W m<sup>-2</sup> to  $-0.13$  W m<sup>-2</sup> (Hossaini et al., 2015; Saiz-Lopez et al., 2023).

39 The oceanic air-sea gas exchange of CHBr<sub>3</sub> is parameterized based on the concentration gradient between surface water  
40 and air and is related to wind speed and sea surface temperature via the transfer velocity (e.g. Nightingale et al., 2000).



41 Due to sparse measurements, marine  $\text{CHBr}_3$  emission estimates are subject to large uncertainties (Laube et al., 2023).  
42  $\text{CHBr}_3$  emission inventories from “bottom-up” approaches (e.g. Quack and Wallace, 2003; Butler et al., 2007; Ziska et  
43 al., 2013; Lennartz et al., 2015; Stemmler et al., 2015; Fiehn et al., 2018) are based on in-situ oceanic data, whereas “top-  
44 down” approaches (e.g. Warwick et al., 2006; Liang et al., 2010; Ordóñez et al., 2012) use in situ atmospheric mixing  
45 ratio measurements. Resulting  $\text{CHBr}_3$  emissions span a large range between 150 and 820 Gg Br yr<sup>-1</sup> (Laube et al., 2023).  
46 The different methods cover e.g., statistical extrapolation of measurement-based data (Ziska et al., 2013; and update in  
47 Fiehn et al., 2018), scaling of emissions to chlorophyll-a satellite observations (Ordóñez et al., 2012), modelling  
48 atmospheric  $\text{CHBr}_3$  with a modular flux in a chemistry climate model (Lennartz et al., 2015), and a data-oriented machine-  
49 learning algorithm (Wang et al., 2019). These studies use limited spatial and temporal data coverage, underrepresenting  
50 seasonal and interannual variations and spatial heterogeneity by averaging concentrations.

51 Oceanic  $\text{CHBr}_3$  is mainly linked to primary production through natural processes such as marine organisms like  
52 macroalgae and phytoplankton (Gschwend et al., 1985; Carpenter and Liss, 2000; Quack et al., 2004). Elevated surface  
53 water concentrations are observed in coastal and shelf waters especially including the eastern boundary upwelling systems  
54 (EBUS) (Quack and Wallace, 2003). Laboratory culture studies of phytoplankton production rates by Tokarczyk and  
55 Moore (1994) and Moore et al. (1996) reported  $\text{CHBr}_3$  increase during the exponential growth phase of phytoplankton.  
56 Those specific growth rates and the corresponding temporal changes in  $\text{CHBr}_3$  concentrations were first applied in a  
57 physical biogeochemical water column model for the tropical Atlantic (Hense and Quack, 2009), and later implemented  
58 in the global biogeochemical HAMBURG Ocean Carbon Cycle model (HAMOCC; Stemmler et al., 2015). Stemmler et al.  
59 (2015) explicitly implemented sources and sinks of marine  $\text{CHBr}_3$  in the three-dimensional ocean biogeochemistry model  
60 HAMOCC. However, they are not fully coupled with the atmosphere, and resulting emissions rely on fixed, prescribed,  
61 extrapolated, observed atmospheric data of Ziska et al. (2013). Since the atmospheric concentrations are regulated by the  
62 oceanic emissions, accurate estimates of atmospheric and oceanic  $\text{CHBr}_3$  variability require such coupling, which can be  
63 achieved using an Earth System Model (ESM).

64 Here, we present the first global model simulation of  $\text{CHBr}_3$  in the fully coupled Norwegian ESM (NorESM2), where  
65  $\text{CHBr}_3$  production is prognostically related to the primary production in the ocean taking natural biological processes into  
66 account. We present results from a historical experiment focusing on the period 1990 to 2014 and compare them with  
67 HalOcat observations (<https://halocat.geomar.de>). Furthermore, we evaluate oceanic  $\text{CHBr}_3$  excess and deficit regions  
68 and use multilinear regression analysis to identify drivers of oceanic and atmospheric  $\text{CHBr}_3$ , as well as  $\text{CHBr}_3$  emission  
69 variations on regional and temporal scales.

## 70 2 Model and Methods

71 We use the latest version of NorESM2 (NorESM2-LM; Seland et al., 2020; Tjiputra et al., 2020), which has participated  
72 in the Coupled Model Intercomparison Project phase 6 (CMIP6) and contributed to the latest assessment report of the  
73 IPCC-AR6 (Masson-Delmotte et al., 2023). The NorESM2 is a fully coupled ESM and is partly based on the Community  
74 ESM Version 2 (Danabasoglu et al., 2020), which is developed by the National Center for Atmospheric Research (NCAR)  
75 in the United States. NorESM2 is an updated version of its original version NorESM1 (Bentsen et al., 2013; Tjiputra et  
76 al., 2013). It consists of a modified version of the Community Atmosphere Model version 6 (CAM6-Nor), the isopycnic  
77 coordinate Bergen Layered Ocean Model (BLOM), the ocean biogeochemistry model isopycnic coordinate HAMOCC  
78 (iHAMOCC), the sea ice model (Community Ice CodE version 5.1.2; CICE5.1.2), the Community Land Model version  
79 5 (CLM5), and the river runoff model (Model for Scale Adaptive River Transport; MOSART). Both BLOM and  
80 iHAMOCC apply a tripolar grid with a horizontal resolution of ~1° and 53 vertical isopycnic layers, while CAM6-Nor  
81 and CLM5 share a common horizontal resolution of ~2° and 32 hybrid-pressure layers (lowest atmospheric layer



82 thickness: ~120 m) and a model top at 3.6 hPa (~40 km altitude). Here, we briefly highlight key features of iHAMOCC  
83 as well as the  $\text{CHBr}_3$  implementation (Section 2.1). The iHAMOCC ocean biogeochemical module is based on the original  
84 work of Maier-Reimer (2012), has gone through several improvements and was later adapted to an isopycnic coordinate  
85 ocean model (Assmann et al., 2010; Tjiputra et al., 2010). The model prognostically simulates inorganic carbon chemistry  
86 following the standard Ocean Model Intercomparison Project (OMIP) protocol. It includes a Nutrient Phytoplankton  
87 Zooplankton Detritus (NPZD) type ecosystem module, where the phytoplankton growth rate is constrained by multi-  
88 nutrient limitation as well as ambient light and temperature. Particulate organic matters produced in the euphotic zone is  
89 exported to the interior with a sinking velocity that increases linearly with depth before it is remineralized back to  
90 inorganic carbon. The NorESM2 is able to simulate the observed large-scale pattern of surface primary productivity as  
91 well as the regional seasonal cycle (Tjiputra et al., 2020).

## 92 2.1 Bromoform module in NorESM2

### 93 2.1.1 Oceanic bromoform

94 The marine  $\text{CHBr}_3$  processes implemented in iHAMOCC comprise of advection ( $adv$ ), production ( $\beta$ ), air-sea gas  
95 exchange ( $F$ ), and three sink terms of: photolysis ( $UV$ ), hydrolysis ( $H$ ) and halogen substitution ( $S$ ), as shown in Eq. (1).  
96 The production and photolysis occur in the euphotic layer (top 100 m depth) of the model, whereas the air-sea gas  
97 exchange is computed in the top-most layer of the ocean (upper 10 m). Advection and other sink terms are calculated  
98 throughout the water column. The change over time of the oceanic  $\text{CHBr}_3$  concentration is modelled as:

$$\frac{[\text{CHBr}_3]}{dt} = adv(\text{CHBr}_3) + \beta - F - UV - H - S. \quad (1)$$

99

100 The parameterizations for the different processes are largely based on Stemmler et al. (2015).  $\text{CHBr}_3$  is produced during  
101 biological production as follows:

$$\beta = \beta_0 * \left( \frac{f_1 * Si(OH)_4}{K_{phy}^{Si(OH)_4} + Si(OH)_4} + \frac{f_2 * K_{phy}^{Si(OH)_4}}{K_{phy}^{Si(OH)_4} + Si(OH)_4} \right), \quad (2)$$

102

103 where diatom and non-diatom contributing factors,  $f_1$  and  $f_2$ , are set equally to 1. In contrast to Stemmler et al. (2015), the  
104 bulk  $\text{CHBr}_3$  production ratio ( $\beta_0$ ) is modified and set to  $2.4 \times 10^{-6} \text{ nmol CHBr}_3 (\text{mmol N})^{-1}$ , based on Kurihara et al. (2012)  
105 and Roy (2010).

106 The air-sea gas exchange is calculated as follows:

$$F = k_w * \left( C_w - \frac{C_a}{H_{bromo}} \right), \quad (3)$$

107

108 where  $C_w$  and  $C_a$  are  $\text{CHBr}_3$  concentrations in the surface ocean and  $\text{CHBr}_3$  mixing ratios in the atmosphere, respectively.  
109 Positive emissions are defined as outgassing to the atmosphere. The temperature-dependent dimensionless Henry's law  
110 solubility constant ( $H_{bromo}$ ) is defined in Moore et al. (1995):

$$H_{bromo} = e^{13.16 - \frac{4973}{SST}}, \quad (4)$$

111

112 with SST the sea-surface temperature in Kelvin.  $k_w$  represents the gas transfer velocity calculated following Nightingale  
113 et al. (2000) using the 10 m surface wind speed ( $u$ ):

$$k_w = (0.222u^2 + 0.33u) * \left( \frac{660}{Sc_{bromo}} \right)^{0.5}. \quad (5)$$



114

115 The Schmidt number ( $Sc_{bromo}$ ) for  $CHBr_3$  is defined in Quack and Wallace (2003) using the sea surface temperature  $SST$   
116 in °C:

$$Sc_{bromo} = 4662.8 - 319.45 * SST + 9.9012 * SST^2 - 0.1159 * SST^3. \quad (6)$$

117

118 The loss term due to photolysis is computed as follows:

$$UV = I_{UV} * \frac{I_0}{I_{ref}} * e^{(-a_w * z)} * [CHBr_3], \quad (7)$$

119

120 where the decay time scale ( $I_{UV}$ )<sup>-1</sup> is set to 30 days (Carpenter and Liss, 2000).  $I_0$  and  $I_{ref}$  are the prognostic incoming UV  
121 radiation (i.e., 30% of shortwave radiation) and annual average irradiance at the surface layer, respectively.  $z$  is the depth  
122 and  $a_w$  is the attenuation coefficient of UV radiation, set to 0.33 m<sup>-1</sup>.

123 The loss term related to hydrolysis is estimated following Stemmler et al. (2015):

$$H = A_1 * e^{(-\frac{E_A}{RT})} * [OH^-] * [CHBr_3], \quad (8)$$

124

125 with  $A_1$ ,  $E_A$ , and  $R$  set to 1.23x10<sup>17</sup> L mol<sup>-1</sup> min<sup>-1</sup>, 107 300 J mol<sup>-1</sup>, and 8.314 J K<sup>-1</sup> mol<sup>-1</sup>, respectively (Washington, 1995).  
126  $T$  is the seawater temperature in Kelvin.

127

128 Degradation due to halogen substitution (Eq. 5-6 of Stemmler et al., 2015):

$$S = L_{ref} * e^{(A_2 * (\frac{1}{T_{ref}} - \frac{1}{T}))} * [CHBr_3], \quad (9)$$

129

130 with  $L_{ref}$  and  $A_2$  set to 7.33x10<sup>-10</sup> s<sup>-1</sup> and 12507.13 K, respectively, and  $T_{ref} = 298$  K.

### 131 2.1.2 Atmospheric $CHBr_3$

132  $CHBr_3$  is implemented as a 3-dimensional tracer in the atmospheric model and is transported by the large-scale  
133 atmospheric circulation and sub-grid scale processes (shallow and deep convection, and boundary layer turbulence). It is  
134 removed in the atmosphere by photolysis:



135

136 and by reaction with the OH radical:



137

138 The reaction rate  $k$  [cm<sup>3</sup> molecules<sup>-1</sup> s<sup>-1</sup>] for the removal of  $CHBr_3$  by OH in

$$\frac{d[CHBr_3]}{dt} = -k * [CHBr_3] * [OH] \quad (12)$$

139

140 is defined as follows:

$$k = 9.0 * 10^{-13} \exp\left(-\frac{360}{T}\right), \quad (13)$$

141



142 with  $T$  the ambient temperature in Kelvin, and  $[\text{CHBr}_3]$  and  $[\text{OH}]$  in molecules  $\text{cm}^{-3}$ . The loss rate of  $\text{CHBr}_3$  by photolysis  
143 can be expressed by

$$\frac{d[\text{CHBr}_3]}{dt} = -I [\text{CHBr}_3], \quad (14)$$

144  
145 where  $I [\text{s}^{-1}]$  depends on the intensity of solar radiation and photo-physical properties of  $\text{CHBr}_3$ . The OH concentration is  
146 a monthly-varying climatology obtained from a Whole Atmosphere Community Climate Model (WACCM) historical  
147 simulation with full tropospheric and stratospheric chemistry (Gettelman et al., 2019).  
148  $\text{CHBr}_3$  in the atmosphere has no other sinks than reaction with OH (annual mean  $\text{CHBr}_3$  lifetime: ~46 days) and photolysis  
149 ( $\text{CHBr}_3$  lifetime: ~23 days) and is not affected by dry or wet deposition.

## 150 2.2 Model setup

151 A historical transient model run from 1850-2014, based on the CMIP6 protocol, was performed following a 500-year  
152 preindustrial spin-up. The coupling of  $\text{CHBr}_3$  between the ocean and the atmosphere is carried out with an hourly time  
153 frequency exchanging the air-sea gas transfer. For analysis of the model climatology as well as for analysis of the model  
154 validation with observations and further analysis of the driving  $\text{CHBr}_3$  factors, daily model output data was averaged over  
155 a period of 25 years (1990-2014) resulting in one mean value for each day of the year. The standard deviation of each  
156 day reflects the variability within this time period. The 1990 to 2014 interval was chosen as most of the observations for  
157 the model validation are within that time period, as compiled in the HalOcAt database (<https://halocat.geomar.de>, last  
158 access: 13.10.2023).

## 159 2.3 Observations: HalOcAt database

160 The HalOcAt database, compiled by Ziska et al. (2013), updated by Fiehn et al. (2018) and by this study, is an observation-  
161 based database for global oceanic and atmospheric data of short-lived halogenated compounds, such as  $\text{CHBr}_3$ . To date,  
162 there are 9369 oceanic and 65179 atmospheric  $\text{CHBr}_3$  measurements listed in 68 oceanic and 156 atmospheric datasets  
163 (campaigns), respectively. The following criteria were applied to the observations in order to be used for model validation:

- 164 - Sampling locations with an ocean bottom depth less than 200 m or closer than 100 km to land were excluded.
- 165 - Sampling depth of oceanic  $\text{CHBr}_3$  measurements had to be within the first 10 m of the water column in order to  
166 be comparable to the  $\text{CHBr}_3$  output of the upper surface ocean model layer (10 m depth).
- 167 - Maximum sampling height of atmospheric  $\text{CHBr}_3$  measurements was set to 30 m altitude.
- 168 - Wherever applicable, individual measurements throughout one day were averaged to result in a daily averaged  
169 surface ocean concentration or atmospheric mixing ratio in order to consider the same temporal resolution as the  
170 daily model output. The coordinates of the respective averaged data points throughout a day were also equally  
171 averaged. These locations were used to compare the observation with the closest grid point of the model output.



172

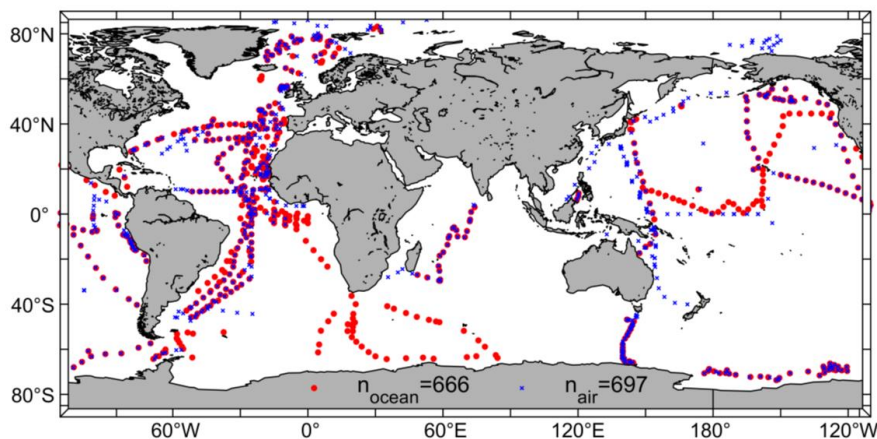


**Figure 1: Locations of oceanic (red, n=666) and atmospheric (blue, n=697) daily mean CHBr<sub>3</sub> observations from the HalOcAt database used to compare to daily mean NorESM2 model output.**

173 After screening the HalOcAt data base with the above-mentioned criteria, the individual oceanic and atmospheric datasets  
174 (including the remaining datapoints) were tested for outliers. The mean from each dataset was calculated and the group  
175 of all average values was tested for outliers. An outlier was defined as an element with more than three standard deviations  
176 from the mean. According to the outlier test for oceanic and atmospheric datasets the corresponding dataset was removed  
177 and not used for further validation of the model.

178 By addressing the mentioned criteria and datasets, we were able to validate the model with 666 daily mean oceanic (5154  
179 individual) and 697 daily mean atmospheric (8411 individual) CHBr<sub>3</sub> observations from the HalOcAt database covering  
180 both hemispheres (northern hemisphere (NH): 61%, southern hemisphere (SH): 39%), from the tropics (0-20°N/S; 36%)  
181 to the polar regions (60-90°N/S; 18%) with most observations in or above the Atlantic Ocean (44%) (Figure 1).

#### 182 2.4 Bromoform excess/deficit calculation

183 The CHBr<sub>3</sub> excess/deficit (balance) rate ( $k_{bal}$ , Eq. (15), pmol m<sup>-2</sup> h<sup>-1</sup>) is the difference between the CHBr<sub>3</sub> production rate  
184 and the sum of different CHBr<sub>3</sub> loss rates, with all rates integrated over the upper 100 m depth):

$$k_{bal} = \sum production\ rate - \sum loss\ rate = k_{\beta} - (k_{UV} + k_F). \quad (15)$$

185

186 The production term is described as the biological oceanic CHBr<sub>3</sub> production rate ( $k_{\beta}$ , Eq. (2)) and the loss term includes  
187 the two fastest loss processes, i.e., photolysis due to UV radiation ( $k_{UV}$ , Eq. (7)) and the loss to the atmosphere via air-sea  
188 gas exchange ( $k_F$ , Eq. (3)). We define a positive  $k_{bal}$  as CHBr<sub>3</sub> excess rate and a negative  $k_{bal}$  as CHBr<sub>3</sub> deficit rate. The  
189 loss terms related to hydrolysis and to halogen substitution are not included as they are several orders of magnitude  
190 smaller than  $k_{UV}$  and  $k_F$ , in the surface ocean.

#### 191 2.5 Bromoform driving factor calculation

192 Different parameters impact the variations of oceanic and atmospheric CHBr<sub>3</sub> values and influence the air-sea gas  
193 exchange. These impacts can vary in magnitude and frequency dependent on local and seasonal conditions. Daily mean  
194 average model output values from 1990-2014 were used to calculate annual and seasonally resolved (DJF, MAM, JJA,  
195 SON) driving factors for oceanic CHBr<sub>3</sub> concentrations ( $Bromo_{oce}$ ), atmospheric CHBr<sub>3</sub> mixing ratios ( $Bromo_{air}$ ) and  
196 CHBr<sub>3</sub> emissions ( $Bromo_{flux}$ ) in three different specific areas (North Atlantic, tropical West Pacific, Southern Ocean),



197 which are presented in Section 3.4. Driving factors for each area, parameter and season were derived using multilinear  
198 regression (MLR) analyses.

199 In order to compare parameters with different magnitudes, input data of each parameter was standardized prior to MLR  
200 analysis by centering to have a mean of 0 and scaled to have a standard deviation of 1. Input data for each parameter  
201 consisted of daily mean averages over the specific area, providing 365 values as basis for annually and ~ 90 values for  
202 seasonally resolved MLR. Equations for MLR calculations were as follows with coefficients  $a$ ,  $b$ ,  $c$ ,  $d$ ,  $e$ ,  $f$ ,  $\text{CHBr}_3$   
203 production ( $\text{Bromo}_{\text{prod}}$ ),  $\text{Bromo}_{\text{oce}}$ ,  $\text{Bromo}_{\text{air}}$  and  $\text{Bromo}_{\text{flux}}$ , as well as the 10 m surface wind speed ( $\text{wind}$ ) and sea surface  
204 temperature ( $\text{SST}$ ):

$$\text{Bromo}_{\text{oce}} = a * \text{SST} + b * \text{wind} + c * \text{Bromo}_{\text{prod}} + d * \text{Bromo}_{\text{flux}} + e * \text{Bromo}_{\text{air}} + f \quad (16)$$

205

$$\text{Bromo}_{\text{flux}} = a * \text{SST} + b * \text{wind} + c * \text{Bromo}_{\text{prod}} + d * \text{Bromo}_{\text{oce}} + e * \text{Bromo}_{\text{air}} + f \quad (17)$$

206

$$\text{Bromo}_{\text{air}} = a * \text{SST} + b * \text{wind} + c * \text{Bromo}_{\text{prod}} + d * \text{Bromo}_{\text{flux}} + e * \text{Bromo}_{\text{oce}} + f \quad (18)$$

207

208 Other oceanic  $\text{CHBr}_3$  loss processes (e.g. photolysis) were neglected in these calculations as the loss due to gas exchange  
209 is ~70 times higher than the loss due to photolysis (data not shown). If the highest resulting coefficient for each season  
210 and MLR is significantly higher than all other coefficients, the corresponding parameter is presented as the main driver  
211 for either  $\text{Bromo}_{\text{oce}}$ ,  $\text{Bromo}_{\text{air}}$  or  $\text{Bromo}_{\text{flux}}$ . If the highest resulting coefficient is not significantly different from the second  
212 or third highest coefficient, more than one coefficient and corresponding parameters are presented as main drivers. Table  
213 1 lists the annual mean coefficients, Table S1 lists the seasonally resolved main drivers.

## 214 3 Results and Discussion

### 215 3.1 Model climatology

216 The annual and seasonal  $\text{CHBr}_3$  oceanic concentrations, atmospheric mixing ratios and emissions reveal significant  
217 spatial variations (Figure 2). The annual global average surface  $\text{CHBr}_3$  concentrations are  $5.04 \text{ pmol L}^{-1}$  (DJF:  
218  $5.36 \text{ pmol L}^{-1}$ , JJA:  $4.86 \text{ pmol L}^{-1}$ ) with highest annual mean concentrations of  $28.37 \text{ pmol L}^{-1}$  in the upwelling region off  
219 the coast of Peru and lowest annual mean concentrations of  $1.37 \text{ pmol L}^{-1}$  in the Gulf of Boothia ( $71^\circ\text{N}$ ,  $91^\circ\text{W}$ ) north of  
220 Canada. The areas with the lowest oceanic  $\text{CHBr}_3$  concentrations are the central parts of the North and the South Pacific  
221 Gyres. Concentrations of surface ocean  $\text{CHBr}_3$  in the entire NH (JJA:  $5.9 \text{ pmol L}^{-1}$  > DJF:  $4.3 \text{ pmol L}^{-1}$ ) and SH (DJF:  
222  $6.1 \text{ pmol L}^{-1}$  > JJA:  $4.1 \text{ pmol L}^{-1}$ ) are generally higher during the respective summer than during the respective winter  
223 season. These distinct differences of oceanic  $\text{CHBr}_3$  concentrations are also due to the higher biological production in  
224 summer (NH:  $335 \text{ pmol m}^{-2} \text{ h}^{-1}$ ; SH:  $371 \text{ pmol m}^{-2} \text{ h}^{-1}$ ) than in winter (NH:  $235 \text{ pmol m}^{-2} \text{ h}^{-1}$ ; SH:  $173 \text{ pmol m}^{-2} \text{ h}^{-1}$ ) as  
225 shown in Fig. S3. The direct link of  $\text{CHBr}_3$  to the biological production applies to the low oceanic  $\text{CHBr}_3$  concentrations  
226 in the North and South Pacific Gyres and to the high oceanic concentrations in the areas of the EBUS.

227 Variations in annual mean atmospheric  $\text{CHBr}_3$  mixing ratios mainly follow the surface ocean concentrations with highest  
228 mixing ratios in the tropics, especially in the EBUS. Global annual average mixing ratios over the ocean are  $0.67 \text{ ppt}$   
229 (DJF:  $0.70 \text{ ppt}$ , JJA:  $0.69 \text{ ppt}$ ) with highest annual mean mixing ratios of  $2.21 \text{ ppt}$  in the south-eastern Pacific upwelling  
230 region off the coast of Peru and lowest annual mean mixing ratios of  $0.13 \text{ ppt}$  over the Persian Gulf. On a global average,  
231 the variability of atmospheric mixing ratios is lower than the variability of  $\text{CHBr}_3$  concentrations in the surface ocean  
232 (Figure 2). During austral winter (JJA), mostly dark and cold conditions increase the lifetime of atmospheric  $\text{CHBr}_3$ ,  
233 which leads to a uniform mixing ratio ( $0.67 \pm 0.05 \text{ ppt}$ ) over the entire Southern Ocean. Similar to oceanic  $\text{CHBr}_3$



234 concentrations, central parts of the North and South Pacific Gyre have low atmospheric  $\text{CHBr}_3$  mixing ratios  
235 ( $0.46 \pm 0.05$  ppt). During austral summer (DJF) atmospheric mixing ratios increase further as strong biological activity  
236 increases surface ocean concentrations, which enhance the oceanic emissions.  
237 Generally, supersaturation of  $\text{CHBr}_3$  in the world's ocean leads to emissions from the ocean to the atmosphere (defined  
238 as positive). Global annual mean emissions are  $268 \text{ pmol m}^{-2} \text{ h}^{-1}$  (DJF:  $294 \text{ pmol m}^{-2} \text{ h}^{-1}$ , JJA:  $253 \text{ pmol m}^{-2} \text{ h}^{-1}$ ) with  
239 highest annual mean emissions of  $953 \text{ pmol m}^{-2} \text{ h}^{-1}$  in the upwelling region off the coast of Peru. In the tropical regions,  
240 annual mean emissions of  $427 \text{ pmol m}^{-2} \text{ h}^{-1}$  between  $10^\circ\text{N}$  and  $10^\circ\text{S}$ , add to atmospheric entrainment of oceanic  $\text{CHBr}_3$   
241 up into the stratosphere (Fiehn et al., 2018; Tegtmeier et al., 2020). Lowest annual mean emissions of  $-1 \text{ pmol m}^{-2} \text{ h}^{-1}$  are  
242 modelled under ice free conditions in the Gulf of Boothia ( $71^\circ\text{N}$ ,  $91^\circ\text{W}$ ) north of Canada (white regions in Figure 2) with  
243 very low oceanic  $\text{CHBr}_3$  production and low seawater temperatures. However, the atmospheric mixing ratios are  
244 comparably high under these conditions. These conditions favour negative emissions, which, according to the results of  
245 our fully coupled ESM, can be seen in the Arctic and Antarctic during winter season, confirming the results by Stemmler  
246 et al. (2015) and Ziska et al. (2013) although with a lower amount.  
247 Generally, the modelled  $\text{CHBr}_3$  emissions are high, where the ocean concentration is high and the elevated emissions lead  
248 to elevated atmospheric mixing ratios. However, due to oceanic transport processes, locations of high oceanic  $\text{CHBr}_3$   
249 emissions do not always coincide with locations of high oceanic  $\text{CHBr}_3$  production (compare Figure 2 and Fig. S3). In  
250 the northern part of the Bay of Bengal ( $>18^\circ\text{N}$ ) e.g., ocean concentrations during DJF are very high (average:  
251  $21.64 \text{ pmol L}^{-1}$ ), while the emissions are not as high compared to other ocean regions, due to low wind speeds. This leads  
252 to a lower atmospheric mixing ratio than expected from the oceanic concentrations and shows that oceanic  $\text{CHBr}_3$   
253 concentrations and emissions as well as atmospheric mixing ratios show regionally different interdependencies, which is  
254 addressed in detail in Section 3.4.  
255

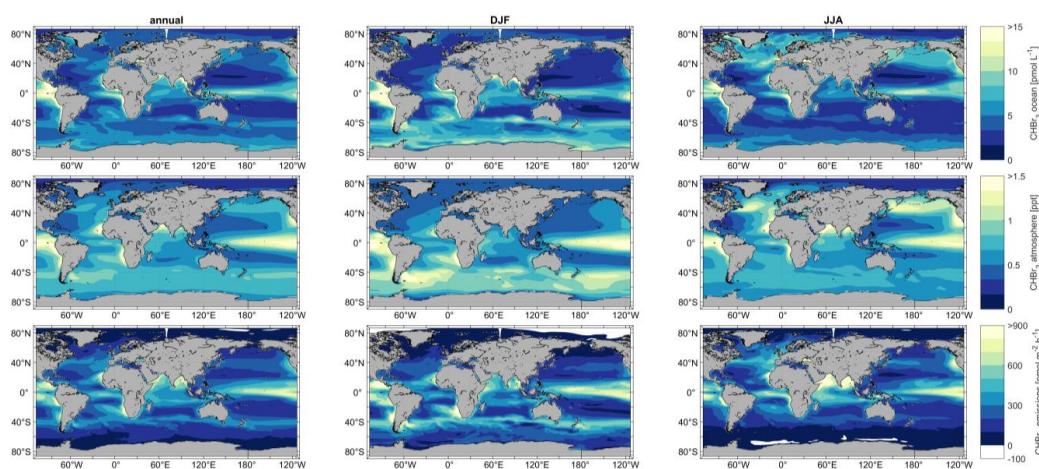


Figure 2: Simulated annual (left), DJF (middle) and JJA (right) mean oceanic surface  $\text{CHBr}_3$  concentrations (upper panel), atmospheric mixing ratios (middle panel) and  $\text{CHBr}_3$  emissions (lower panel) for the period 1990-2014.

### 256 3.2 Model validation with observations

257 The annual median surface oceanic  $\text{CHBr}_3$  concentration (Figure 3a) from the 666 daily mean observations is  $3.65 \text{ pmol L}^{-1}$   
258 with a 25<sup>th</sup> and 75<sup>th</sup> percentile of 2.19 and  $6.16 \text{ pmol L}^{-1}$ , respectively (min:  $0.05 \text{ pmol L}^{-1}$ , max:  $28.21 \text{ pmol L}^{-1}$ , mean:  
259  $5.02 \text{ pmol L}^{-1}$ ). The global annual median surface oceanic  $\text{CHBr}_3$  concentration from the model using only locations  
260 corresponding with an existing observation is  $6.00 \text{ pmol L}^{-1}$  with a 25<sup>th</sup> and 75<sup>th</sup> percentile of 4.23 and  $8.10 \text{ pmol L}^{-1}$ ,





261 respectively (min: 1.39 pmol L<sup>-1</sup>, max: 24.25 pmol L<sup>-1</sup>, mean: 6.61 pmol L<sup>-1</sup>). These results indicate that the model values  
 262 are in the range with observed concentrations of oceanic CHBr<sub>3</sub>. While the median concentration of the model is higher  
 263 than the median of the observations, all validated model data points fall within the full range of the observations. The  
 264 model data cover a grid of ~100 km resolution, which leads to a smoothing of the values, whereas observational data is  
 265 local daily mean point data.

266 The median CHBr<sub>3</sub> atmospheric mixing ratio (Figure 3b) from the 697 daily mean observations is 1.17 ppt with a 25<sup>th</sup>  
 267 and 75<sup>th</sup> percentile of 0.78 and 1.71 ppt, respectively (min: 0.03 ppt, max: 9.80 ppt). The global median atmospheric  
 268 mixing ratio of CHBr<sub>3</sub> from the model at locations with observations is 0.69 ppt with a 25<sup>th</sup> and 75<sup>th</sup> percentile of 0.49  
 269 and 0.90 ppt, respectively (min: 0.22 ppt, max: 2.70 ppt). This comparison shows that the observed atmospheric mixing  
 270 ratios of CHBr<sub>3</sub> are in the same magnitude but generally higher than those from the model output. While our model  
 271 experiment focuses on natural CHBr<sub>3</sub> production by phytoplankton, other sources as coastal macroalgae (Carpenter and  
 272 Liss, 2000) and anthropogenic sources, such as power plant cooling (Maas et al., 2021) or desalination plants (Agus et  
 273 al., 2009), may explain parts of the higher global annual median observational data of 41%. Jia et al. (2023) calculated

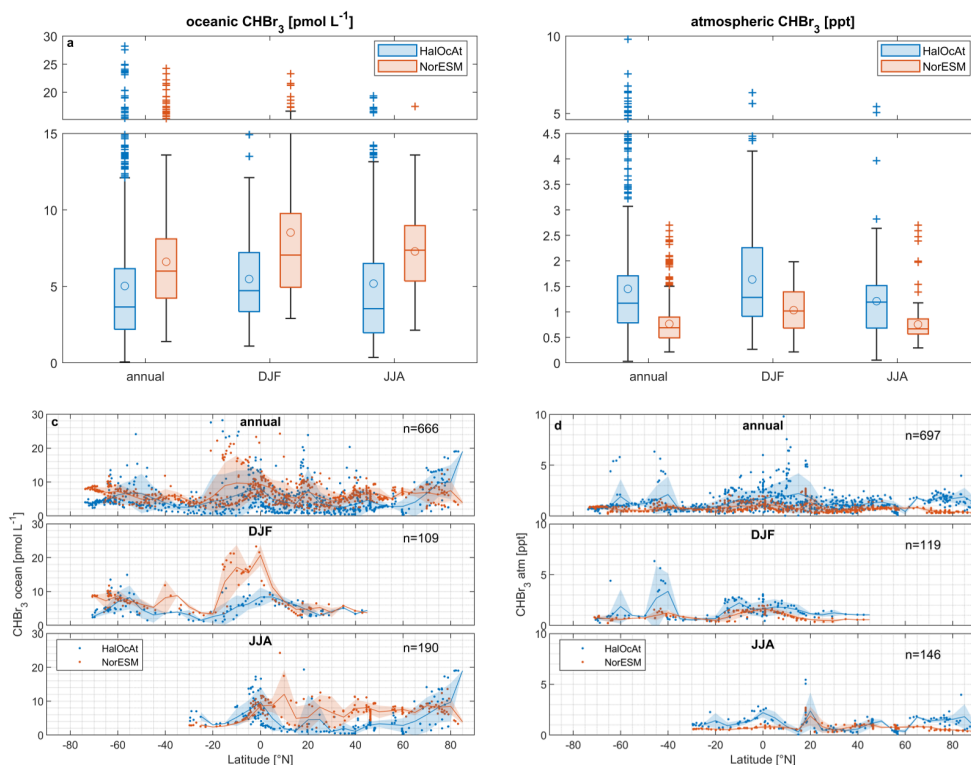


**Figure 3:** Boxplot comparison of NorESM2 model results with HalOcat observations for oceanic (a) and atmospheric CHBr<sub>3</sub> (b), c: zonal mean oceanic CHBr<sub>3</sub> comparison annually and in DJF and JJA, d: zonal mean atmospheric CHBr<sub>3</sub> comparison annually and in DJF and JJA. Shaded areas are standard deviations from 5° zonal bin averages. Boxplots (left) have a break in the y axis to increase readability of the figure. The line inside the box represents the median value, the circle the mean value, the boxes show the first to third quartile, and the whiskers illustrate the highest and lowest values that are not outliers. The plus signs represent outliers.

274 an increase of global CHBr<sub>3</sub> emissions of 31.5% when including anthropogenic emissions, which partly explains also the  
 275 lower observed atmospheric mixing ratios in the model compared to the observations.

276 Figure 3 also shows a more detailed comparison between observations and model data in 5° meridional binned averages  
 277 (shaded areas) for oceanic (Figure 3c) and atmospheric (Figure 3d) CHBr<sub>3</sub> on annual basis as well as in JJA and DJF.  
 278 The modelled data compare well with observations of oceanic CHBr<sub>3</sub> (Figure 3c) on annual basis over the 5° latitudinal



279 bins. In the HalOcat database, there are no oceanic and atmospheric observations available north of 50°N and south of  
280 30°S during boreal (DJF) and austral winter (JJA), respectively, which highlights the need of model data to entirely  
281 describe spatially and temporally resolved CHBr<sub>3</sub> (see also Fiehn et al., 2018). During DJF, the model overestimates the  
282 measured concentrations between 20°N and 5°S. During JJA, averaged model concentrations in the NH (10°N – 60°N)  
283 are slightly higher than the averaged observations. These discrepancies could indicate a missing process understanding,  
284 revealing lower oceanic production or additional loss processes.

285 With all data available, the 5° latitudinal averaged atmospheric CHBr<sub>3</sub> observations have a large spread in the tropics  
286 resulting in a high standard deviation (Figure 3d). The model results in this region are uniform with a much lower standard  
287 deviation. During boreal winter (DJF) atmospheric CHBr<sub>3</sub> observations and model results show a good agreement, with  
288 an exception at 40-50°S. In this latitude range, observational atmospheric CHBr<sub>3</sub> mixing ratios (>3 ppt, Figure 3d) were  
289 recorded between 24° and 60° W in the South Atlantic in 2007 (Gebhardt, 2008). Gebhardt (2008) reports enhanced  
290 biological production in the Argentinian shelf-break zone (55°-60° W) with elevated chlorophyll-*a* concentration up to  
291 4.5 µg L<sup>-1</sup>. These values suggest also a high production of CHBr<sub>3</sub> and subsequent high emissions to the atmosphere. The  
292 prevailing westerly winds, transported the CHBr<sub>3</sub> enriched air masses eastward to the remote South Atlantic region in  
293 2007, while in the model lower biological production entails lower atmospheric mixing ratios compared to the  
294 observations. During boreal summer (JJA) very good agreement between atmospheric observations and model results is  
295 obtained between 10°N and 60°N. North of 60°N, the model underestimates the measured atmospheric mixing ratios in  
296 the polar region. Local meteorological and biological conditions (e.g. high wind speed, distinct phytoplankton blooms)  
297 are averaged by the model to a resolution of ~100 km. Averaging data over time or space leads to lower values (e.g. gas  
298 emissions, Bates and Merlivat, 2001), which explains lower modelled atmospheric mixing ratios compared to the  
299 observations. These local and short term temporal variations contribute to the discrepancy in atmospheric values at global  
300 scale as well as potential anthropogenic CHBr<sub>3</sub> emissions (Jia et al., 2023). Furthermore, discrepancies between model  
301 results and observations also point to missing process understanding, which helps to improve our understanding of the  
302 biogeochemical cycling of CHBr<sub>3</sub>.

### 303 3.3 Excess and deficit regions of oceanic bromoform

304 In most of the world's surface oceans CHBr<sub>3</sub> production and loss rates are balanced on an annual average with a  $k_{bal}$  close  
305 to zero (e.g. North and South Pacific, top panel of Figure 4). The equator region experiences a strong excess rate (positive  
306  $k_{bal}$ ) on annual average with values up to 300 pmol m<sup>-2</sup> h<sup>-1</sup> showing higher CHBr<sub>3</sub> production than loss of CHBr<sub>3</sub> in the  
307 upper ocean, caused by strong primary production (Fig. S3) in the equatorial upwelling. Surface currents transport the  
308 CHBr<sub>3</sub> enriched surface water masses away from the equator, while experiencing loss of CHBr<sub>3</sub> to the atmosphere.  
309 Therefore, adjacent marine areas north and south of the equator experience a deficit rate (negative  $k_{bal}$ ) of CHBr<sub>3</sub> (blue  
310 areas, Figure 4), as no production balances the loss. The seasonality of  $k_{bal}$  is pronounced in the extratropics (bottom  
311 panels of Figure 4). In these regions, a CHBr<sub>3</sub> excess rate is observed mainly during summer and a CHBr<sub>3</sub> deficit rate  
312 mainly during winter in the respective hemispheres. A high  $k_{\beta}$  (elevated biological production) and a low  $k_F$  (weak  
313 emissions to the atmosphere) caused by lower winds during summer, lead to a higher CHBr<sub>3</sub> surface ocean concentration  
314 in summer compared to winter time (Figure 2). During winter in both hemispheres, lower biological activity (low  $k_{\beta}$ ) and  
315 elevated wind speed (high  $k_F$ ) decrease the CHBr<sub>3</sub> production and increase the emissions to the atmosphere, which leads  
316 to a CHBr<sub>3</sub> deficit rate. These results reveal seasonal as well as spatial differences in parameters (driving factors), which  
317 influence CHBr<sub>3</sub> concentrations in the world's ocean.

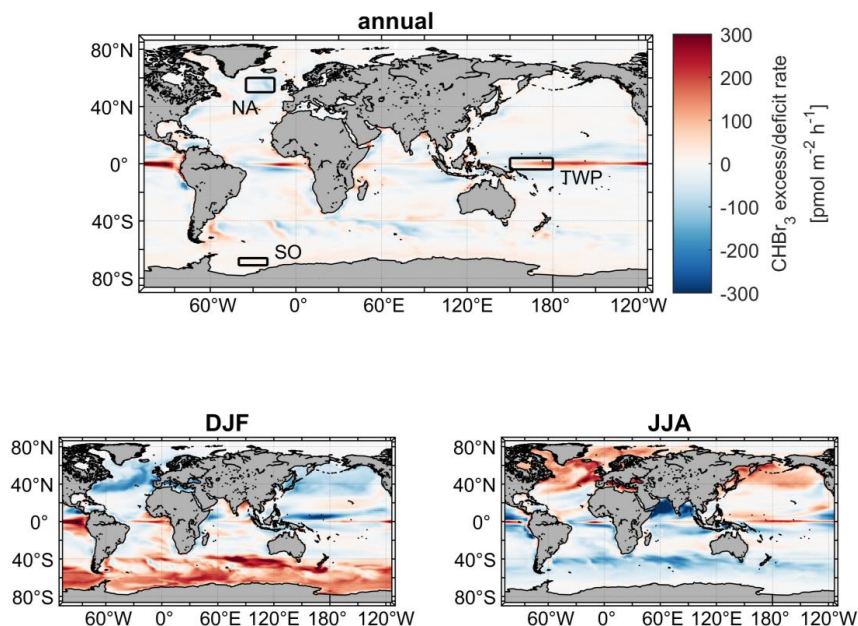


**Figure 4: Mean CHBr<sub>3</sub> excess/deficit rates on annual (top) and seasonal (DJF: bottom left; JJA: bottom right) basis. Three rectangles in the top figure illustrate locations of case studies. NA: North Atlantic; TWP: Tropical West Pacific; SO: Southern Ocean.**

318 In the following subsection, we selected three different case study areas, indicated in Figure 4, in order to contrast the  
319 driving factors of the variations of oceanic and atmospheric CHBr<sub>3</sub> on regional and temporal scales:

- 320 - North Atlantic, with an annual mean CHBr<sub>3</sub> deficit rate ( $k_{bal} = -33 \text{ pmol m}^{-2} \text{ h}^{-1}$ )
- 321 - Tropical West Pacific, with an annual mean CHBr<sub>3</sub> excess rate ( $k_{bal} = +32 \text{ pmol m}^{-2} \text{ h}^{-1}$ )
- 322 - Southern Ocean, with negative emissions during the respective winter season ( $k_{bal} = +15 \text{ pmol m}^{-2} \text{ h}^{-1}$ )

### 323 3.4 Driving factors of bromoform on regional and temporal scales

324 This section investigates the seasonal changes of oceanic and atmospheric CHBr<sub>3</sub> and other parameters in three  
325 contrasting regions. Daily means of oceanic CHBr<sub>3</sub> concentrations, production, emissions, balance (as defined in Eq.  
326 (15)), atmospheric mixing ratios as well as SST and wind speed, in the North Atlantic, tropical West Pacific and Southern  
327 Ocean over an entire year reveal large differences between the regions (Figure 5). With MLR analysis, the main driving  
328 factors of oceanic and atmospheric CHBr<sub>3</sub> variability and its emissions in each region and season are investigated.



329

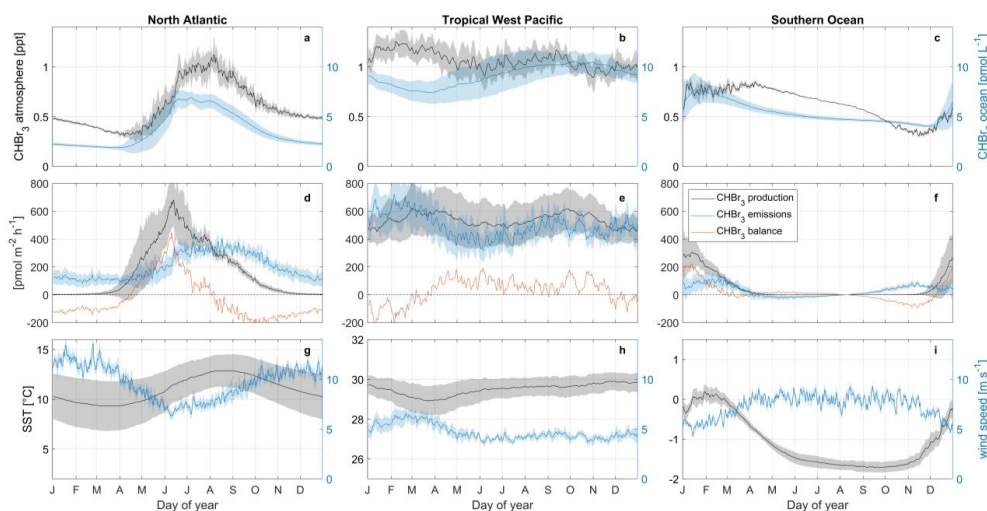


**Figure 5: Seasonal changes of oceanic and atmospheric CHBr<sub>3</sub> (upper panel, a-c), CHBr<sub>3</sub> production, emissions and balance (middle panel, d-f), SST and wind speed (bottom panel, g-i), in the North Atlantic (left), tropical west Pacific (middle) and Southern Ocean (right). Shaded area is one standard deviation of the average value in the corresponding area. Note: y-limits for SST are not similar in between the three regions in order to increase readability of the figure.**

330

### 331 North Atlantic

332 The North Atlantic region (50°N – 60°N, 15°W – 35°W) is characterized by a strong seasonal cycle of both oceanic  
333 CHBr<sub>3</sub> concentrations and atmospheric mixing ratios (Figure 5a). The magnitude of the cycle is strongest among the three  
334 investigated regions in this study (compare with Figure 5b,c). Oceanic CHBr<sub>3</sub> concentrations are on average 3.64 pmol L<sup>-1</sup>  
335 with a minimum concentration of 1.87 pmol L<sup>-1</sup> during end of March and a maximum concentration of 6.93 pmol L<sup>-1</sup>  
336 during July. Atmospheric mixing ratios show a similar seasonal cycle, shifted by one month, with average values of  
337 0.60 ppt, a minimum mixing ratio of 0.30 ppt during April and a maximum mixing ratio of 1.12 ppt during August. Figure  
338 5d shows, that the CHBr<sub>3</sub> emissions (199±91 pmol m<sup>-2</sup> h<sup>-1</sup>) follow the pattern of both oceanic and atmospheric values.  
339 The seasonal cycle of CHBr<sub>3</sub> production (171±191 pmol m<sup>-2</sup> h<sup>-1</sup>) is similar to the cycle of CHBr<sub>3</sub> concentration, while the  
340 sharp peak in May/June when the spring phytoplankton bloom evolves in the North Atlantic, is not reflected in the oceanic  
341 concentrations. The strong seasonality in CHBr<sub>3</sub> production leads to a CHBr<sub>3</sub> excess rate during summer (JJA:  
342 103 pmol m<sup>-2</sup> h<sup>-1</sup>) and a CHBr<sub>3</sub> deficit rate in winter time (DJF: -114 pmol m<sup>-2</sup> h<sup>-1</sup>), respectively (Figure 5d).

343 The MLR analysis indicates, that on an annual basis, variations in atmospheric mixing ratios are mainly associated with  
344 CHBr<sub>3</sub> ocean concentrations (Table 1, R<sup>2</sup>=0.89, p-value<0.05) and vice versa (Figure 6a,d). A higher surface water CHBr<sub>3</sub>  
345 concentration increases the emissions to the atmosphere resulting in increasing atmospheric mixing ratios. According to  
346 the MLR analysis on a seasonal basis, oceanic CHBr<sub>3</sub> concentrations are mainly driven by the oceanic production during  
347 MAM (R<sup>2</sup>=0.93, p-value<0.05) and SON (R<sup>2</sup>=0.99, p-value<0.05) (Table S1), which increases from March to June  
348 sharply to 680 pmol m<sup>-2</sup> h<sup>-1</sup> before gradually decreasing in SON (Figure 5d). Annually, atmospheric mixing ratios are  
349 mainly driven by the oceanic concentration (Figure 6d, Table 1, R<sup>2</sup>=0.89, p-value<0.05). This is also true on a seasonal  
350 basis except for the winter (DJF) season, where SST is the main (indirect) factor influencing the atmospheric mixing ratio  
351 variations (Table S1, R<sup>2</sup>=0.95, p-value<0.05), as lower SSTs increase the solubility of CHBr<sub>3</sub> and hardly any oceanic  
352 CHBr<sub>3</sub> production occurs. Thus, the emissions of CHBr<sub>3</sub> decrease, even during comparably high wind speeds, which  
353 leads to a decreasing atmospheric mixing ratio. CHBr<sub>3</sub> emissions are mainly driven by oceanic concentrations on an



354 annual basis (Figure 6g, Table 1,  $R^2=0.81$ ,  $p$ -value $<0.05$ ). The MLR results further indicate that the driving factors are  
355 highly variable, when looking on a seasonal basis. During spring (MAM), wind speed, SST, and  $\text{CHBr}_3$  production are  
356 almost equally driving the emissions (Table S1). During this season,  $\text{CHBr}_3$  emissions are pretty constant at  
357  $130\pm 29$   $\text{pmol m}^{-2} \text{h}^{-1}$  (Figure 5d).  $\text{CHBr}_3$  production and SSTs slightly increase in spring, and an increase of the emissions  
358 to the atmosphere is expected. However, emissions stay constant as surface wind speed decreases and lower the emissions.  
359 This regional and seasonal pattern explicitly illustrates the interaction of different conditions influencing the  $\text{CHBr}_3$   
360 emissions. During summer (JJA), low winds and a high oceanic  $\text{CHBr}_3$  concentration equally influence the increasing  
361 emissions (Table S1). In contrast to spring, higher SSTs (lower solubility) are only of minor importance during JJA. In  
362 autumn and winter, decreasing emissions are mainly driven by decreasing SSTs and, in DJF, additionally by high  
363 atmospheric mixing ratios (in comparison to oceanic concentrations), which additionally dampens the emissions (Table  
364 S1).

### 365 Tropical West Pacific

366 Figure 4 shows that the equatorial regions of the Atlantic and Pacific Oceans generally have positive  $k_{bal}$  and therefore  
367 are a source of oceanic  $\text{CHBr}_3$ , which is transported to other oceanic regions.  $\text{CHBr}_3$  ocean concentrations in the tropical  
368 West Pacific ( $4^\circ\text{S} - 4^\circ\text{N}$ ,  $150^\circ\text{E} - 180^\circ\text{E}$ ) show a reduced seasonal cycle in comparison to the above discussed North  
369 Atlantic region (Figure 5b). Oceanic concentrations are on average  $9.11$   $\text{pmol L}^{-1}$  which is significantly higher than  
370 average concentrations in the North Atlantic while the seasonal amplitude (min:  $7.42$   $\text{pmol L}^{-1}$  in March; max:  
371  $10.58$   $\text{pmol L}^{-1}$  in October) is less pronounced.  $\text{CHBr}_3$  production ( $536\pm 42$   $\text{pmol m}^{-2} \text{h}^{-1}$ ),  $\text{CHBr}_3$  emissions  
372 ( $492\pm 84$   $\text{pmol m}^{-2} \text{h}^{-1}$ ) and atmospheric mixing ratios ( $1.07\pm 0.08$  ppt) show hardly any seasonality (Figure 5b, e). The  
373 same is true for SST ( $29.50\pm 0.28$   $^\circ\text{C}$ ) and wind speed ( $4.71\pm 0.76$   $\text{m s}^{-1}$ ) (Figure 5h). The  $\text{CHBr}_3$  balance is positive  
374 throughout the whole year except for DJF (Figure 5e). During this period high wind speed leads to higher emission than  
375 production rates and induces low oceanic concentrations which results in a  $\text{CHBr}_3$  deficit. However, this deficit does not  
376 compensate for the  $\text{CHBr}_3$  excess during the rest of the year leading to an overall positive  $k_{bal}$  of  $32$   $\text{pmol m}^{-2} \text{h}^{-1}$ .  
377 MLR analysis shows that the wind speed is the main factor influencing the variations of oceanic  $\text{CHBr}_3$  concentrations  
378 ( $R^2=0.51$ ,  $p$ -value $<0.05$ ),  $\text{CHBr}_3$  atmospheric mixing ratios ( $R^2=0.74$ ,  $p$ -value $<0.05$ ), and  $\text{CHBr}_3$  emissions ( $R^2=0.73$ ,  
379  $p$ -value $<0.05$ ) on an annual basis (Figure 6b,e,h, Table 1) in the equatorial region. During JJA and SON  $\text{CHBr}_3$  production  
380 drives the  $\text{CHBr}_3$  concentrations (Table S1, JJA:  $R^2=0.43$ ,  $p$ -value $<0.05$ , SON:  $R^2=0.51$ ,  $p$ -value $<0.05$ ) which increases  
381 from  $477$   $\text{pmol m}^{-2} \text{h}^{-1}$  in July to  $618$   $\text{pmol m}^{-2} \text{h}^{-1}$  by the end of September. This results in an increase of oceanic  $\text{CHBr}_3$   
382 concentrations as all other parameters stay constant during that period.

### 383 Southern Ocean

384 The selected Southern Ocean region ( $71^\circ\text{S} - 66^\circ\text{S}$ ,  $40^\circ\text{W} - 20^\circ\text{W}$ ) experiences water temperatures, which are negative  
385 almost any time around the year (Figure 5i). Average temperature is  $-1.08^\circ\text{C}$  with minimum temperatures of  $-1.71^\circ\text{C}$  in  
386 September (late winter) and maximum temperatures of  $+0.19^\circ\text{C}$  in January/February (late summer). Wind speed in this  
387 region is nearly constant throughout the year ( $7.33$   $\text{m s}^{-1}$ ) with lower average wind speed of  $5.76$   $\text{m s}^{-1}$  only during austral  
388 summer (DJF, Figure 5h). Oceanic  $\text{CHBr}_3$  concentrations in the Southern Ocean region are on average higher  
389 ( $5.38$   $\text{pmol L}^{-1}$ ) than in the North Atlantic region with maximum concentrations ( $7.74$   $\text{pmol L}^{-1}$ ) in January and lowest  
390 concentrations ( $4.04$   $\text{pmol L}^{-1}$ ) end of December. This sharp increase of  $\text{CHBr}_3$  concentrations within two months  
391 demonstrates the limited biological activity period, visible in the  $\text{CHBr}_3$  production rate (Figure 5f). Due to decreasing  
392 SSTs as well as a decreased day length,  $\text{CHBr}_3$  production rates are almost zero from May to October and sharply increase  
393 up to  $306$   $\text{pmol m}^{-2} \text{h}^{-1}$  in January. Atmospheric mixing ratios are highest (max:  $0.85$  ppt) from January to beginning of  
394 April but decline very slowly (Figure 5c) under low light levels, until they reach their minimum of  $0.31$  ppt in November.



395 Constant high atmospheric mixing ratios, due to light limitations in combination with very low SST, and decreasing  
396 oceanic CHBr<sub>3</sub> concentrations, after the short summer bloom in DJF, influence the switch from positive emissions to  
397 negative emissions between April and July (Figure 5f). CHBr<sub>3</sub> is in excess during times of CHBr<sub>3</sub> production (DJF) and  
398 is almost balanced during the autumn and wintertime (April – September, Figure 5f). On annual basis, CHBr<sub>3</sub> is almost  
399 balanced in this region with a slight excess of 15 pmol m<sup>-2</sup> h<sup>-1</sup>.  
400

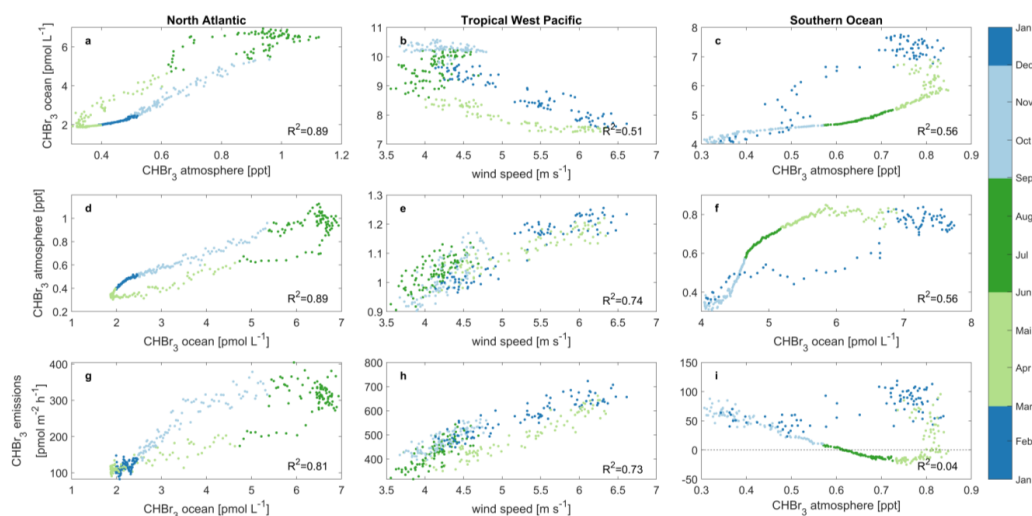


**Figure 6:** Main drivers of oceanic CHBr<sub>3</sub> concentrations (a, b, c), atmospheric mixing ratios (d, e, f) and CHBr<sub>3</sub> emissions (g, h, i) in the North Atlantic (a, d, g), tropical West Pacific (b, e, h) and Southern Ocean (c, f, i). Different colours denote different seasons of the year. Each data point represents a daily mean average over the specific case study area.

401 Overall, the MLR analysis confirms that atmospheric mixing ratios are the main factor influencing the variations of  
402 oceanic concentrations on annual basis (Figure 6c, Table 1, R<sup>2</sup>=0.56, p-value<0.05). CHBr<sub>3</sub> production is the driving  
403 factor for the ocean concentration during autumn (MAM, Table S1). During this time CHBr<sub>3</sub> production decreases and  
404 so does the ocean concentration Figure 5c,f). The atmospheric mixing ratio is mainly driven by oceanic concentrations at  
405 times with high oceanic CHBr<sub>3</sub> concentrations (DJF: R<sup>2</sup>=0.88, p-value<0.05) and by SST during cold winter times (JJA:  
406 R<sup>2</sup>=0.95, p-value<0.05) (Table S1). In winter during low light levels, atmospheric CHBr<sub>3</sub> reactions are reduced, which  
407 increases the lifetime of atmospheric CHBr<sub>3</sub>. Additionally, low SSTs increase the solubility of oceanic CHBr<sub>3</sub>. These two  
408 conditions favour the overall dampening of the CHBr<sub>3</sub> sea-to-air emissions during winter (JJA). During the summer in  
409 DJF CHBr<sub>3</sub> emissions are mainly driven by SST (Table S1, R<sup>2</sup>=0.60, p-value<0.05), as the solubility of CHBr<sub>3</sub> in the  
410 ocean significantly decreases due to the increasing sea surface temperatures. After this short summer period, temperatures  
411 decline in autumn (MAM) and increase the solubility of oceanic CHBr<sub>3</sub>, which results in decreased emissions (Figure  
412 5f,i). During winter (JJA) and spring (SON), surface temperatures and oceanic CHBr<sub>3</sub> concentrations stay low and  
413 therefore, increasing emissions are mainly driven by decreasing atmospheric mixing ratios.

414

415 These results demonstrate the benefits of simulating CHBr<sub>3</sub> in a fully coupled ESM configuration to calculate driving  
416 factors for different parameters on temporal and spatial basis. Studying the influence of one or more parameters on the  
417 variability of other parameters in the model is not realistic when using prescribed oceanic concentrations or atmospheric  
418 mixing ratios. Investigating the CHBr<sub>3</sub> cycling in different locations and different time scales helps to understand their  
419 interconnection and to better integrate their results in today's as well as in a future climate.

420



421

422

423 **Table 1: Annual coefficients of predictors for each MLR in the different case studies. Bold coefficients are the highest value**  
 424 **within a MLR analysis of one parameter and region and act as indicator for the driving factors of the predicted parameter**  
 425 **(Eq. (16)-(18)).**

	Predictor parameter	North Atlantic	Tropical West Pacific	Southern Ocean
Ocean concentration	Wind speed	-0.02	<b>-0.96</b>	-0.10
	SST	<0.01	<0.01	<0.01
	Atm. mixing ratio	<b>0.68</b>	0.19	<b>0.60</b>
	CHBr <sub>3</sub> production	0.39	0.13	0.53
	CHBr <sub>3</sub> emissions	<0.01	<0.01	<0.01
Atmospheric mixing ratio	Wind speed	0.29	<b>0.94</b>	0.55
	SST	0.32	<0.01	<0.01
	Ocean concentration	<b>0.93</b>	0.12	<b>1.07</b>
	CHBr <sub>3</sub> production	<0.01	0.02	<0.01
	CHBr <sub>3</sub> emissions	<0.01	<0.01	<0.01
CHBr <sub>3</sub> emissions	Wind speed	0.20	<b>1.27</b>	0.21
	SST	0.67	0.50	0.53
	Ocean concentration	<b>0.83</b>	0.16	1.00
	CHBr <sub>3</sub> production	<0.01	0.10	<0.01
	Atm. mixing ratio	-0.32	-0.02	<b>-1.22</b>

426

427

### 428 3.5 Global bromoform emission inventories

429 A comparison of our modelled versus published global CHBr<sub>3</sub> emissions are presented in Figure 7. Global annual CHBr<sub>3</sub>  
 430 emissions from top-down approaches are 449 Gg yr<sup>-1</sup>, 528 Gg yr<sup>-1</sup> and 592 Gg yr<sup>-1</sup> based on calculations from Liang et  
 431 al. (2010), Ordóñez et al. (2012) and Warwick et al. (2006), respectively. These inventories are about two to eight times  
 432 higher than calculated annual emissions from bottom-up approaches, which are in the range of 76 Gg yr<sup>-1</sup> (Stemmler et  
 433 al., 2015) to 238 Gg yr<sup>-1</sup> (Lennartz et al., 2015). Our results (214 Gg yr<sup>-1</sup>) are similar to emission estimates published by  
 434 Ziska et al. (2013) of 215 Gg yr<sup>-1</sup> but significantly higher than the 76 Gg yr<sup>-1</sup> estimate by Stemmler et al. (2015), which  
 435 is based on the oceanic CHBr<sub>3</sub> observations from HalOcAt.

436 As we apply a 2.38 higher CHBr<sub>3</sub> production rate in the ocean as Stemmler et al. (2015), we simulate a production rate  
 437 of 0.88 Gmol yr<sup>-1</sup> compared to 0.37 Gmol yr<sup>-1</sup> by Stemmler et al. (2015). Our emissions (214 Gg yr<sup>-1</sup>) are 2.82 times  
 438 higher (Figure 7, global values) compared to the emission estimate (76 Gg yr<sup>-1</sup>) from Stemmler et al. (2015). Our model  
 439 adaption is based on the higher bulk CHBr<sub>3</sub> production ratio ( $\beta_0$ ) according to Kurihara et al. (2012) and Roy (2010) (see  
 440 Section 2.1.1). This production rate is at the higher end of published values. Therefore, the resulting CHBr<sub>3</sub> production  
 441 can be seen as an upper limit.



442 Comparing bottom-up and top-down approaches, the annual  $\text{CHBr}_3$  emissions account for ~47% (105  $\text{Gg yr}^{-1}$ ) and ~66%  
443 (351  $\text{Gg yr}^{-1}$ ), respectively, from the tropics ( $20^\circ\text{S} - 20^\circ\text{N}$ , Figure 7), which account for ~37% of global oceanic surface,  
444 underlining the tropics as the most important source region of  $\text{CHBr}_3$  of the earth.  
445 Emissions in the middle latitudes ( $20$  to  $50^\circ\text{N/S}$ ) of the NH and SH show a similar distinction between top-down and  
446 bottom-up approaches. However, the annual  $\text{CHBr}_3$  emissions are only half that of the tropics. Natural open ocean  
447 emission estimates from our study are proportional to the surface area between NH and SH in the middle latitudes. This  
448 relationship is reversed for the top-down approach estimates. Top-down emission estimates are higher in the NH  
449 compared to the SH although the oceanic surface area is lower in the NH (17%) compared to the SH (26%). This indicates  
450 the strong influence of coastal emissions on observational atmospheric mixing ratios used in top-down approaches.  
451 In the high latitudes ( $50$ - $90^\circ\text{N/S}$ ), emissions of bottom-up approaches are in the same range (SH) and even higher (NH)

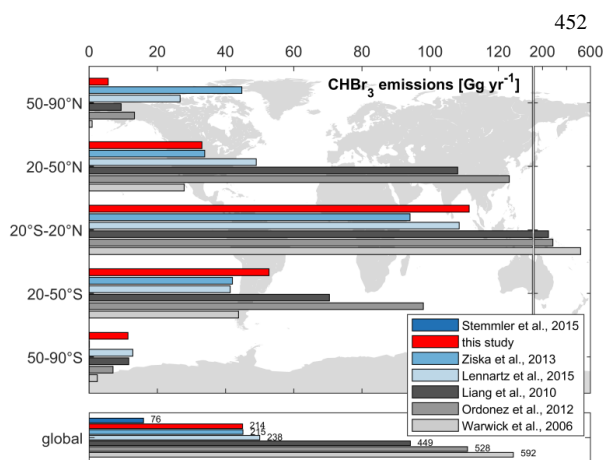


**Figure 7: Comparison of global and latitudinally binned annual  $\text{CHBr}_3$  emissions from different studies. Grey and blue bars denote top-down and bottom-up approaches, respectively.**

467 in Stemmler et al. (2015) are biased to the ice-free summer months, with higher atmospheric mixing ratios, thus artificially  
468 dampening the emissions from the ocean to the atmosphere during winter seasons. Due to the influence of the annually  
469 fixed prescribed atmospheric mixing ratios in Stemmler et al. (2015), negative emissions are more pronounced between  
470  $50^\circ\text{N/S}$  and  $70^\circ\text{N/S}$  up to  $-100 \text{ pmol m}^{-2} \text{ h}^{-1}$  at  $\sim 60^\circ\text{N/S}$ . Our lesser negative emissions in the coupled ESM approach  
471 appear more realistic as they are not based on summer biased prescribed values.

472

473 Our global  $\text{CHBr}_3$  emission inventory indicates distinct differences to the top-down approaches reflecting only 40%-50%  
474 of global emissions calculated by Liang et al. (2010), Ordóñez et al. (2012) and Warwick et al. (2006). Atmospheric  
475  $\text{CHBr}_3$  values in the top-down approaches are higher than the calculated atmospheric mixing ratios from our fully coupled  
476 model analysis. They include elevated coastal (Scenario A and C, Liang et al., 2010), including anthropogenic (Ordóñez  
477 et al., 2012) sources, which may partly explain the discrepancy.

478 An additional explanation for the overall higher atmospheric mixing ratios of  $\text{CHBr}_3$  from observations could be that  
479 observations from coastal areas (100 km within the coastline) were excluded from this study and are not represented in  
480 the model, as they are difficult to quantify (e.g. tide-dependent  $\text{CHBr}_3$  emissions of macroalgae) with a horizontal model  
481 resolution of  $1^\circ$ . However, coastal emissions lead to higher atmospheric mixing ratios of  $\text{CHBr}_3$  (Fuhlbrügge et al., 2013;  
482 Fuhlbrügge et al., 2016; Hepach et al., 2016), which can be transported to remote open ocean regions, while these higher  
483 observational values are not included in the model results (Figure 3).

452 compared to top-down approaches (Figure 7). In  
the northern polar region (8% of global oceanic  
surface area),  $\text{CHBr}_3$  emissions from our study  
account for 3% (6  $\text{Gg yr}^{-1}$ ) of global emissions  
and are significantly lower than the other two  
bottom-up approaches from Lennartz et al.  
(2015) (11%, 27  $\text{Gg yr}^{-1}$ ) and Ziska et al. (2013)  
(21%, 45  $\text{Gg yr}^{-1}$ ), which appears mainly due to  
the resolved seasonality within our study.  
According to the HalOcAt database, no  
measurements are recorded from November to  
February and from May to September north of  
 $50^\circ\text{N}$  in the NH and south of  $50^\circ\text{S}$  in the SH,  
respectively. Therefore, the prescribed  
atmospheric values in Ziska et al. (2013) but also





484 Another explanation for the underestimation of the modelled atmospheric mixing ratios compared to observations is the  
485 use of air-sea gas exchange parameterizations, whose uncertainty is estimated to be 25% (Wanninkhof, 2007) and may  
486 be underestimated up to 75% (Yang et al., 2022) at low wind speeds.

#### 487 **4 Conclusions and Outlook**

488 Our study is the first one to derive oceanic and atmospheric  $\text{CHBr}_3$  concentrations, as well as emissions, from a fully  
489 coupled ESM simulation. The model prognostically simulates oceanic  $\text{CHBr}_3$  production by phytoplankton and includes  
490 oceanic  $\text{CHBr}_3$  loss due to air-sea gas exchange, photolysis, hydrolysis and halogen substitution. Atmospheric loss of  
491  $\text{CHBr}_3$  is described by photolysis and the reaction with OH. We validate the model results with more than 5,100 oceanic  
492 and 8,400 atmospheric observations from the HalOcat database. The simulated global mean  $\text{CHBr}_3$  emission rate (214  
493  $\text{Gg yr}^{-1}$ ) is in the range of previously published bottom-up approaches (76-238  $\text{Gg yr}^{-1}$ ), but significantly lower than top-  
494 down approaches (449-592  $\text{Gg yr}^{-1}$ ). The model allows to realistically resolve seasonal and spatial variations and to  
495 identify different drivers of oceanic and atmospheric  $\text{CHBr}_3$  variability on regional and seasonal scales. Our results  
496 indicate that only during high productive seasons a consequently high  $\text{CHBr}_3$  production drives high oceanic  $\text{CHBr}_3$   
497 concentrations. During low productive seasons, relatively high atmospheric mixing ratios suppress the gas exchange and  
498 consequently influence variations in oceanic  $\text{CHBr}_3$  concentrations. In tropical regions (e.g. tropical West Pacific) with a  
499 small seasonal cycle, but high oceanic concentrations and atmospheric mixing ratios, wind speed is the main factor driving  
500 the variability of oceanic and atmospheric  $\text{CHBr}_3$  and its emissions. The results clearly indicate the benefit of a fully  
501 coupled ocean-atmosphere-biogeochemistry ESM. In earlier modelling studies, prescribed, fixed atmospheric or oceanic  
502 values were applied, which bias the seasonal impact of different factors on oceanic and atmospheric  $\text{CHBr}_3$  and  
503 subsequently induce additional uncertainties to the magnitude of  $\text{CHBr}_3$  emissions.

504 Our fully coupled ocean atmosphere approach resolves natural biogenic oceanic and atmospheric  $\text{CHBr}_3$  including their  
505 emissions at relatively high temporal and spatial model resolution. Validation with observational data shows good  
506 agreement for large scale spatial patterns and we attribute the remaining model-data differences to missing coastal  
507 sources, which are not implemented in the model. Comparison with other published  $\text{CHBr}_3$  inventories indicates that  
508 approaches without seasonality lack to resolve  $\text{CHBr}_3$  emissions especially in high latitudes.

509 Our results demonstrate the potential for applying a fully coupled ESM to elucidate the primary drivers of the observed  
510  $\text{CHBr}_3$  concentrations and emissions variability across spatial and temporal scales. Moreover, this model set-up allows  
511 to implement additional oceanic derived VLS in order to further investigate their influence on the atmospheric chemistry.  
512 The dissociation of open ocean natural derived  $\text{CHBr}_3$  from coastal area derived  $\text{CHBr}_3$  in this study reveal that coastal  
513 derived  $\text{CHBr}_3$  influences open ocean atmospheric mixing ratios. Therefore, implementing natural coastal next to  
514 anthropogenic sources and concurrent model resolution increase in these areas will help to further close the gap of  
515 published  $\text{CHBr}_3$  emission estimates between bottom-up and top-down approaches. Long-term future changes in  $\text{CHBr}_3$   
516 dynamics under various scenarios should be investigated with a fully coupled ESM, to study the impact of climate change  
517 on  $\text{CHBr}_3$  dynamics, e.g. in the Arctic, associated with loss of sea-ice and its climate feedback through interaction with  
518 ozone chemistry.

519

520 **Data availability.** Observational data can be downloaded from <https://halocat.geomar.de>. Model data will be archived  
521 and will be made available upon request.

522

523

524



525

526 **Author contributions.**

527 DB wrote the manuscript and led the discussion with contributions from all authors. DB analysed the model simulations  
528 and prepared the graphics. JFT and DJLO implemented the CHBr<sub>3</sub> model code changes in NorESM2 in discussion with  
529 BQ and all other authors. JFT carried out the model runs. KK led this project and initiated the research idea for this study.  
530

531 **Competing interests.** The authors declare that they have no conflict of interest.

532

533 **Acknowledgements.** This work was financed by the Research Council of Norway through the KeyCLIM project  
534 (295046) within the KLIMAFORSK/POLARFORSK program. Resources for the model simulations and data storage  
535 were provided by Sigma2 - the National Infrastructure for High Performance Computing and Data Storage in Norway.  
536

537 **References**

538 Agus, E., Voutchkov, N., and Sedlak, D. L.: Disinfection by-products and their potential impact on the quality of water  
539 produced by desalination systems: A literature review, *Desalination*, 237, 214-237, 10.1016/j.desal.2007.11.059, 2009.

540 Assmann, K. M., Bentsen, M., Segschneider, J., and Heinze, C.: An isopycnic ocean carbon cycle model, *Geoscientific*  
541 *Model Development*, 3, 143-167, DOI 10.5194/gmd-3-143-2010, 2010.

542 Bates, N. R. and Merlivat, L.: The influence of short-term wind variability on air-sea CO  
543 exchange, *Geophysical Research Letters*, 28, 3281-3284, Doi 10.1029/2001gl012897, 2001.

544 Butler, J. H., King, D. B., Lobert, J. M., Montzka, S. A., Yvon-Lewis, S. A., Hall, B. D., Warwick, N. J., Mondeel, D. J.,  
545 Aydin, M., and Elkins, J. W.: Oceanic distributions and emissions of short-lived halocarbons, *Global Biogeochemical*  
546 *Cycles*, 21, Artn Gb1023  
547 10.1029/2006gb002732, 2007.

548 Carpenter, L. J. and Liss, P. S.: On temperate sources of bromoform and other reactive organic bromine gases, *Journal of*  
549 *Geophysical Research-Atmospheres*, 105, 20539-20547, Doi 10.1029/2000jd900242, 2000.

550 Danabasoglu, G., Lamarque, J. F., Bacmeister, J., Bailey, D. A., DuVivier, A. K., Edwards, J., Emmons, L. K., Fasullo,  
551 J., Garcia, R., Gettelman, A., Hannay, C., Holland, M. M., Large, W. G., Lauritzen, P. H., Lawrence, D. M., Lenaerts, J.  
552 T. M., Lindsay, K., Lipscomb, W. H., Mills, M. J., Neale, R., Oleson, K. W., Otto-Bliesner, B., Phillips, A. S., Sacks,  
553 W., Tilmes, S., van Kampenhout, L., Vertenstein, M., Bertini, A., Dennis, J., Deser, C., Fischer, C., Fox-Kemper, B.,  
554 Kay, J. E., Kinnison, D., Kushner, P. J., Larson, V. E., Long, M. C., Mickelson, S., Moore, J. K., Nienhouse, E., Polvani,  
555 L., Rasch, P. J., and Strand, W. G.: The Community Earth System Model Version 2 (CESM2), *Journal of Advances in*  
556 *Modeling Earth Systems*, 12, e2019MS001916, ARTN e2019MS001916  
557 10.1029/2019MS001916, 2020.

558 Daniel, J. S., Solomon, S., Portmann, R. W., and Garcia, R. R.: Stratospheric ozone destruction: The importance of  
559 bromine relative to chlorine, *Journal of Geophysical Research-Atmospheres*, 104, 23871-23880, Doi  
560 10.1029/1999jd900381, 1999.

561 Dorf, M., Butler, J. H., Butz, A., Camy-Peyret, C., Chipperfield, M. P., Kritten, L., Montzka, S. A., Simmes, B., Weidner,  
562 F., and Pfeilsticker, K.: Long-term observations of stratospheric bromine reveal slow down in growth, *Geophysical*  
563 *Research Letters*, 33, Artn L24803  
564 10.1029/2006gl027714, 2006.

565 Fiehn, A., Quack, B., Stemmler, I., Ziska, F., and Krüger, K.: Importance of seasonally resolved oceanic emissions for  
566 bromoform delivery from the tropical Indian Ocean and west Pacific to the stratosphere, *Atmospheric Chemistry and*  
567 *Physics*, 18, 11973-11990, 10.5194/acp-18-11973-2018, 2018.

568 Fuhlbrügge, S., Krüger, K., Quack, B., Atlas, E., Hepach, H., and Ziska, F.: Impact of the marine atmospheric boundary  
569 layer conditions on VLSL abundances in the eastern tropical and subtropical North Atlantic Ocean, *Atmospheric*  
570 *Chemistry and Physics*, 13, 6345-6357, 10.5194/acp-13-6345-2013, 2013.



- 571 Fuhlbrügge, S., Quack, B., Tegtmeier, S., Atlas, E., Hepach, H., Shi, Q., Raimund, S., and Krüger, K.: The contribution  
572 of oceanic halocarbons to marine and free tropospheric air over the tropical West Pacific, *Atmospheric Chemistry and*  
573 *Physics*, 16, 7569-7585, 10.5194/acp-16-7569-2016, 2016.
- 574 Gebhardt, S.: Biogenic emission of halocarbons, Mainz, Univ., Diss., 2008, 10.25358/openscience-2211, 2008.
- 575 Gettelman, A., Mills, M. J., Kinnison, D. E., Garcia, R. R., Smith, A. K., Marsh, D. R., Tilmes, S., Vitt, F., Bardeen, C.  
576 G., McInerny, J., Liu, H. L., Solomon, S. C., Polvani, L. M., Emmons, L. K., Lamarque, J. F., Richter, J. H., Gnanville,  
577 A. S., Bacmeister, J. T., Phillips, A. S., Neale, R. B., Simpson, I. R., DuVivier, A. K., Hodzic, A., and Randel, W. J.: The  
578 Whole Atmosphere Community Climate Model Version 6 (WACCM6), *Journal of Geophysical Research-Atmospheres*,  
579 124, 12380-12403, 10.1029/2019jd030943, 2019.
- 580 Gschwend, P. M., Macfarlane, J. K., and Newman, K. A.: Volatile halogenated organic compounds released to seawater  
581 from temperate marine macroalgae, *Science*, 227, 1033-1035, 10.1126/science.227.4690.1033, 1985.
- 582 Hense, I. and Quack, B.: Modelling the vertical distribution of bromoform in the upper water column of the tropical  
583 Atlantic Ocean, *Biogeosciences*, 6, 535-544, DOI 10.5194/bg-6-535-2009, 2009.
- 584 Hepach, H., Quack, B., Tegtmeier, S., Engel, A., Bracher, A., Fuhlbrügge, S., Galgani, L., Atlas, E. L., Lampel, J., Friess,  
585 U., and Krüger, K.: Biogenic halocarbons from the Peruvian upwelling region as tropospheric halogen source,  
586 *Atmospheric Chemistry and Physics*, 16, 12219-12237, 10.5194/acp-16-12219-2016, 2016.
- 587 Hossaini, R., Chipperfield, M. P., Montzka, S. A., Rap, A., Dhomse, S., and Feng, W.: Efficiency of short-lived halogens  
588 at influencing climate through depletion of stratospheric ozone, *Nature Geoscience*, 8, 186-190, 10.1038/Ngeo2363,  
589 2015.
- 590 Jia, Y., Hahn, J., Quack, B., Jones, E., Brehon, M., and Tegtmeier, S.: Anthropogenic Bromoform at the Extratropical  
591 Tropopause, *Geophysical Research Letters*, 50, e2023GL102894, ARTN e2023GL102894  
592 10.1029/2023GL102894, 2023.
- 593 Kurihara, M., Iseda, M., Ioriya, T., Horimoto, N., Kanda, J., Ishimaru, T., Yamaguchi, Y., and Hashimoto, S.: Brominated  
594 methane compounds and isoprene in surface seawater of Sagami Bay: Concentrations, fluxes, and relationships with  
595 phytoplankton assemblages, *Marine Chemistry*, 134, 71-79, 10.1016/j.marchem.2012.04.001, 2012.
- 596 Laube, J. C., Tegtmeier, S., Fernandez, R. P., Harrison, J., Hu, L., Krummel, P., Mahieu, E., Park, S., and Western, L.:  
597 Update on Ozone-Depleting Substances (ODSs) and Other Gases of Interest to the Montreal Protocol, 978-9914-733-97-  
598 6, 2023.
- 599 Law, K., Sturges, W., Blake, D., Blake, N., Burkholder, J., Butler, J., Cox, R., Haynes, P., Ko, M., and Kreher, K.:  
600 Halogenated very short-lived substances, Chapter 2 in: *Scientific Assessment of Ozone Depletion: 2006*, Global Ozone  
601 Research and Monitoring Project–Report No. 50, World Meteorological Organization, Geneva, Switzerland, 572, 2007.
- 602 Lennartz, S. T., Kryzstofiak, G., Marandino, C. A., Sinnhuber, B. M., Tegtmeier, S., Ziska, F., Hossaini, R., Krüger, K.,  
603 Montzka, S. A., Atlas, E., Oram, D. E., Keber, T., Bönisch, H., and Quack, B.: Modelling marine emissions and  
604 atmospheric distributions of halocarbons and dimethyl sulfide: the influence of prescribed water concentration vs.  
605 prescribed emissions, *Atmospheric Chemistry and Physics*, 15, 11753-11772, 10.5194/acp-15-11753-2015, 2015.
- 606 Liang, Q., Stolarski, R. S., Kawa, S. R., Nielsen, J. E., Douglass, A. R., Rodriguez, J. M., Blake, D. R., Atlas, E. L., and  
607 Ott, L. E.: Finding the missing stratospheric Br: a global modeling study of CHBr<sub>3</sub> and CH<sub>2</sub>Br<sub>2</sub>, *Atmospheric Chemistry*  
608 *and Physics*, 10, 2269-2286, DOI 10.5194/acp-10-2269-2010, 2010.
- 609 Maas, J., Tegtmeier, S., Jia, Y., Quack, B., Durgadoo, J. V., and Biastoch, A.: Simulations of anthropogenic bromoform  
610 indicate high emissions at the coast of East Asia, *Atmospheric Chemistry and Physics*, 21, 4103-4121, 10.5194/acp-21-  
611 4103-2021, 2021.
- 612 Maier-Reimer, E.: Geochemical cycles in an ocean general circulation model. Preindustrial tracer distributions, *Global*  
613 *Biogeochemical Cycles*, 7, 645-677, 10.1029/93gb01355, 2012.
- 614 Masson-Delmotte, V., Zhai, P., Pirani, A., Connors, S. L., Péan, C., Berger, S., Caud, N., Chen, Y., Goldfarb, L., Gomis,  
615 M. I., Huang, M., Leitzell, K., Lonnoy, E., Matthews, J. B. R., Maycock, T. K., Waterfield, T., Yelekçi, O., Yu, R., Zhou,  
616 B., and Ipcc: Annex I: Observational Products, in: *Climate Change 2021 – The Physical Science Basis*, Cambridge  
617 University Press, Cambridge, United Kingdom and New York, NY, USA, 2061-2086, 10.1017/9781009157896.015,  
618 2023.



- 619 Montzka, S. A., Reimann, S., Engel, A., Kruger, K., Sturges, W. T., Blake, D., Dorf, M., Fraser, P., Froidevaux, L., and  
620 Jucks, K.: Ozone-depleting substances (ODSs) and related chemicals (chapter 1), 2011.
- 621 Moore, R. M., Geen, C. E., and Tait, V. K.: Determination of Henry's Law constants for a suite of naturally occurring  
622 halogenated methanes in seawater, *Chemosphere*, 30, 1183-1191, 10.1016/0045-6535(95)00009-w, 1995.
- 623 Moore, R. M., Webb, M., Tokarczyk, R., and Wever, R.: Bromoperoxidase and iodoperoxidase enzymes and production  
624 of halogenated methanes in marine diatom cultures, *Journal of Geophysical Research-Oceans*, 101, 20899-20908, Doi  
625 10.1029/96jc01248, 1996.
- 626 Navarro, M. A., Atlas, E. L., Saiz-Lopez, A., Rodriguez-Lloveras, X., Kinnison, D. E., Lamarque, J. F., Tilmes, S., Filus,  
627 M., Harris, N. R., Meneguz, E., Ashfold, M. J., Manning, A. J., Cuevas, C. A., Schauffler, S. M., and Donets, V.: Airborne  
628 measurements of organic bromine compounds in the Pacific tropical tropopause layer, *Proc Natl Acad Sci U S A*, 112,  
629 13789-13793, 10.1073/pnas.1511463112, 2015.
- 630 Nightingale, P. D., Malin, G., Law, C. S., Watson, A. J., Liss, P. S., Liddicoat, M. I., Boutin, J., and Upstill-Goddard, R.  
631 C.: In situ evaluation of air-sea gas exchange parameterizations using novel conservative and volatile tracers, *Global  
632 Biogeochemical Cycles*, 14, 373-387, Doi 10.1029/1999gb900091, 2000.
- 633 Ordóñez, C., Lamarque, J. F., Tilmes, S., Kinnison, D. E., Atlas, E. L., Blake, D. R., Sousa Santos, G., Brasseur, G., and  
634 Saiz-Lopez, A.: Bromine and iodine chemistry in a global chemistry-climate model: description and evaluation of very  
635 short-lived oceanic sources, *Atmospheric Chemistry and Physics*, 12, 1423-1447, 10.5194/acp-12-1423-2012, 2012.
- 636 Papanastasiou, D. K., McKeen, S. A., and Burkholder, J. B.: The very short-lived ozone depleting substance CHBr  
637 (bromoform): revised UV absorption spectrum, atmospheric lifetime and ozone depletion potential, *Atmospheric  
638 Chemistry and Physics*, 14, 3017-3025, 10.5194/acp-14-3017-2014, 2014.
- 639 Quack, B. and Wallace, D. W. R.: Air-sea flux of bromoform: Controls, rates, and implications, *Global Biogeochemical  
640 Cycles*, 17, 10.1029/2002gb001890, 2003.
- 641 Quack, B., Atlas, E., Petrick, G., Stroud, V., Schauffler, S., and Wallace, D. W. R.: Oceanic bromoform sources for the  
642 tropical atmosphere, *Geophysical Research Letters*, 31, Artn L23s05  
643 10.1029/2004gl020597, 2004.
- 644 Roy, R.: Short-term variability in halocarbons in relation to phytoplankton pigments in coastal waters of the central  
645 eastern Arabian Sea, *Estuarine Coastal and Shelf Science*, 88, 311-321, 10.1016/j.ecss.2010.04.011, 2010.
- 646 Saiz-Lopez, A., Fernandez, R. P., Li, Q., Cuevas, C. A., Fu, X., Kinnison, D. E., Tilmes, S., Mahajan, A. S., Gomez  
647 Martin, J. C., Iglesias-Suarez, F., Hossaini, R., Plane, J. M. C., Myhre, G., and Lamarque, J. F.: Natural short-lived  
648 halogens exert an indirect cooling effect on climate, *Nature*, 618, 967-973, 10.1038/s41586-023-06119-z, 2023.
- 649 Sala, S., Bönisch, H., Keber, T., Oram, D. E., Mills, G., and Engel, A.: Deriving an atmospheric budget of total organic  
650 bromine using airborne in situ measurements from the western Pacific area during SHIVA, *Atmospheric Chemistry and  
651 Physics*, 14, 6903-6923, 10.5194/acp-14-6903-2014, 2014.
- 652 Salawitch, R. J.: Atmospheric chemistry: biogenic bromine, *Nature*, 439, 275-277, 10.1038/439275a, 2006.
- 653 Sinnhuber, B. M., Sheode, N., Sinnhuber, M., Chipperfield, M. P., and Feng, W.: The contribution of anthropogenic  
654 bromine emissions to past stratospheric ozone trends: a modelling study, *Atmospheric Chemistry and Physics*, 9, 2863-  
655 2871, DOI 10.5194/acp-9-2863-2009, 2009.
- 656 Stemmler, I., Hense, I., and Quack, B.: Marine sources of bromoform in the global open ocean - global patterns and  
657 emissions, *Biogeosciences*, 12, 1967-1981, 10.5194/bg-12-1967-2015, 2015.
- 658 Tegtmeier, S., Atlas, E., Quack, B., Ziska, F., and Krüger, K.: Variability and past long-term changes of brominated very  
659 short-lived substances at the tropical tropopause, *Atmospheric Chemistry and Physics*, 20, 7103-7123, 10.5194/acp-20-  
660 7103-2020, 2020.
- 661 Tjiputra, J. F., Assmann, K., Bentsen, M., Bethke, I., Otterå, O. H., Sturm, C., and Heinze, C.: Bergen Earth system model  
662 (BCM-C): model description and regional climate-carbon cycle feedbacks assessment, *Geoscientific Model  
663 Development*, 3, 123-141, DOI 10.5194/gmd-3-123-2010, 2010.



- 664 Tjiputra, J. F., Schwinger, J., Bentsen, M., Morée, A. L., Gao, S., Bethke, I., Heinze, C., Goris, N., Gupta, A., He, Y. C.,  
665 Oliivié, D., Seland, O., and Schulz, M.: Ocean biogeochemistry in the Norwegian Earth System Model version 2  
666 (NorESM2), *Geoscientific Model Development*, 13, 2393-2431, 10.5194/gmd-13-2393-2020, 2020.
- 667 Tokarczyk, R. and Moore, R. M.: Production of Volatile Organohalogenes by Phytoplankton Cultures, *Geophysical  
668 Research Letters*, 21, 285-288, Doi 10.1029/94gl00009, 1994.
- 669 Villamayor, J., Iglesias-Suarez, F., Cuevas, C. A., Fernandez, R. P., Li, Q. Y., Abalos, M., Hossaini, R., Chipperfield, M.  
670 P., Kinnison, D. E., Tilmes, S., Lamarque, J. F., and Saiz-Lopez, A.: Very short-lived halogens amplify ozone depletion  
671 trends in the tropical lower stratosphere, *Nature Climate Change*, 13, 554-+, 10.1038/s41558-023-01671-y, 2023.
- 672 Wang, S. Y., Kinnison, D., Montzka, S. A., Apel, E. C., Hornbrook, R. S., Hills, A. J., Blake, D. R., Barletta, B., Meinardi,  
673 S., Sweeney, C., Moore, F., Long, M., Saiz-Lopez, A., Fernandez, R. P., Tilmes, S., Emmons, L. K., and Lamarque, J.  
674 F.: Ocean Biogeochemistry Control on the Marine Emissions of Brominated Very Short-Lived Ozone-Depleting  
675 Substances: A Machine-Learning Approach, *Journal of Geophysical Research-Atmospheres*, 124, 12319-12339,  
676 10.1029/2019jd031288, 2019.
- 677 Wanninkhof, R.: The Impact of Different Gas Exchange Formulations and Wind Speed Products on Global Air-Sea CO<sub>2</sub>  
678 Fluxes, in: *Transport at the Air-Sea Interface*, edited by: Garbe, C. S., Handler, R. A., and Jähne, B., *Environmental  
679 Science and Engineering*, Springer Berlin Heidelberg, Berlin, Heidelberg, 1-23, 10.1007/978-3-540-36906-6\_1, 2007.
- 680 Warwick, N. J., Pyle, J. A., Carver, G. D., Yang, X., Savage, N. H., O'Connor, F. M., and Cox, R. A.: Global modeling  
681 of biogenic bromocarbons, *Journal of Geophysical Research-Atmospheres*, 111, Artn D24305  
682 10.1029/2006jd007264, 2006.
- 683 Washington, J. W.: Hydrolysis Rates of Dissolved Volatile Organic-Compounds - Principles, Temperature Effects and  
684 Literature-Review, *Ground Water*, 33, 415-424, DOI 10.1111/j.1745-6584.1995.tb00298.x, 1995.
- 685 Yang, M. X., Bell, T. G., Bidlot, J. R., Blomquist, B. W., Butterworth, B. J., Dong, Y. X., Fairall, C. W., Landwehr, S.,  
686 Marandino, C. A., Miller, S. D., Saltzman, E. S., and Zavarisky, A.: Global Synthesis of Air-Sea CO  
687 Transfer Velocity Estimates From Ship-Based Eddy Covariance Measurements, *Front. Mar. Sci.*, 9, ARTN 826421  
688 10.3389/fmars.2022.826421, 2022.
- 689 Ziska, F., Quack, B., Abrahamsson, K., Archer, S. D., Atlas, E., Bell, T., Butler, J. H., Carpenter, L. J., Jones, C. E.,  
690 Harris, N. R. P., Hepach, H., Heumann, K. G., Hughes, C., Kuss, J., Krüger, K., Liss, P., Moore, R. M., Orlikowska, A.,  
691 Raimund, S., Reeves, C. E., Reifenhäuser, W., Robinson, A. D., Schall, C., Tanhua, T., Tegtmeier, S., Turner, S., Wang,  
692 L., Wallace, D., Williams, J., Yamamoto, H., Yvon-Lewis, S., and Yokouchi, Y.: Global sea-to-air flux climatology for  
693 bromoform, dibromomethane and methyl iodide, *Atmospheric Chemistry and Physics*, 13, 8915-8934, 10.5194/acp-13-  
694 8915-2013, 2013.  
695